Energy dependence of fission product yields in the second-chance fission region

M. E. Gooden,[1,*] R. C. Malone,[2] T. A. Bredeweg,[1] E. M. Bond,[1] S. W. Finch,[3,4] C. R. Howell,[3,4] Krishichayan,[3,4] A. P. D. Ramirez,[2] J. A. Silano,[2] M. A. Stoyer,[2] A. P. Tonchev,[2,3] W. Tornow,[3,4] D. Vieira,[1] and J. B. Wilhelmy[1]

[1]*Los Alamos National Laboratory, Los Alamos, New Mexico 87545, USA*

[2]*Lawrence Livermore National Laboratory, Livermore, California 94550, USA*

[3]*Duke University, Durham, North Carolina 27705, USA*

[4]*Triangle Universities Nuclear Laboratory, Durham, North Carolina 27705, USA*

(Received 12 September 2023; accepted 5 January 2024; published 2 April 2024)

An extensive dataset of cumulative fission product yields has been generated under a joint collaboration between Los Alamos National Laboratory (LANL), Lawrence Livermore National Laboratory (LLNL), and the Triangle Universities Nuclear Laboratory (TUNL). The energy dependence of the cumulative yield for a select number of high-yield fission products has been measured using quasimonoenergetic neutrons with energies between 5.5 and 11.0 MeV. This is in addition to previously published data covering 0.5–4.5 and 14.8 MeV. The absolute number of fissions was determined during the irradiation period using dual-fission ionization chambers, and the fission products were measured postactivation by whole target γ-ray spectroscopy. This paper presents the absolute cumulative fission product yields as a function of incident neutron energy from the neutron-induced fission of ^{235}U, ^{238}U, and ^{239}Pu isotopes at four incident energies in the second-chance fission region and compares them with existing literature values. Corrections relevant to this collaboration's previously published data are also discussed.

DOI: 10.1103/PhysRevC.109.044604

I. INTRODUCTION

Nuclear fission is a large-amplitude collective phenomenon in which a heavy parent nucleus splits into two daughter nuclei either spontaneously or as a result of induced fission. The distribution of fragment masses following fission is one of the most basic quantities that has been observed since the discovery of fission by Hahn and Strassmann in 1938 [1]. Since then, fission has been a test bed for nearly all of nuclear physics and has broad applications such as estimation of decay heat and delayed neutron emission in nuclear reactors, studies of the reactor antineutrino anomaly, radio-isotope production for medical applications, development of advanced reactor and transmutation systems, fission in the galactic chemical evolution, and national security. In recent years, the importance of fission has led to a resurgence in experimental and theoretical efforts to understand and measure fission observables to ever higher precision. The most obvious observable from fission is the fission product yields (FPYs) and their dependence on the energy of the incident neutron.

The current evaluated FPY data files contain only three neutron energy groups: thermal, fast, and 14 MeV. The fast neutron energy is nominally defined as ≈0.5–2 MeV, which is in the region of the peak of the fission neutron energy distribution. For some actinides, such as ^{239}Pu, the experimental FPY data are almost nonexistent in the neutron energy range between fast to 14 MeV. In 2010, a series of papers [2–4] presented a reanalysis of cumulative FPY data. For the three major actinides (^{235}U, ^{238}U, and ^{239}Pu) these papers highlighted the existing data, identified gaps present in the data, and, most importantly, showed that there existed a possible dependence on incident neutron energy to the cumulative fission yields of certain fission products. Evaluations of available FPY data by Chadwick *et al.* [5] and Thompson *et al.* [6] presented compelling evidence for a positive energy dependence for the fission product yield of ^{147}Nd from neutron-induced fission of ^{239}Pu in the low-energy region between 0.2 and 2 MeV incident neutron energy. These data came from measurements performed with fast reactors and critical assemblies and were shown to exhibit a positive energy dependence of about 4% per MeV over this energy region, as shown in Fig. 1. In addition to the question of FPY's energy dependence in the fission spectrum region, discrepancies existed for measurements at 14 MeV [3,4], with a near absence of data between those two regions.

Since 2011, our collaboration has undertaken experimental measurements of the energy evolution of the long-lived (chain) FPYs from neutron-induced fission of ^{235}U, ^{238}U, and ^{239}Pu using quasimonoenergetic neutrons. Our FPY results show that cumulative chain yields are strongly dependent on the target nucleus and the incident neutron energy [7]. The high accuracy of the FPY measurements over the energy range of 0.58 to 14.8 MeV confirmed the anomalous energy dependence suggested by Chadwick and Thompson [5,6]. For example, the experimental results for some high-yield fission products such as ^{95,97}Zr, ^{99}Mo, ^{140}Ba, ^{143}Ce, and ^{147}Nd, show a positive-energy trend for $E_n < 5$ MeV. This trend

*m_gooden@lanl.gov

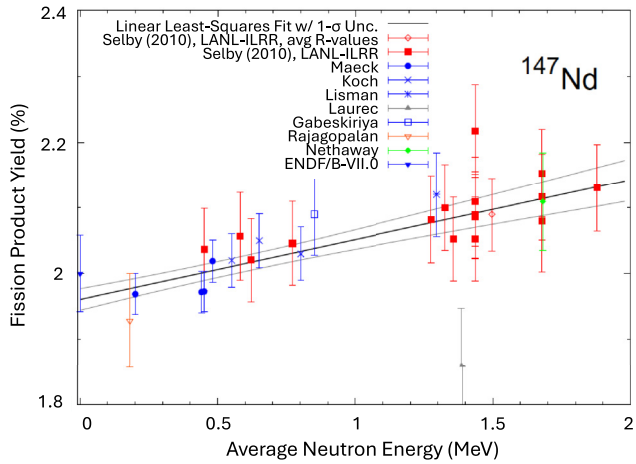

FIG. 1. Existing low-energy fission product yield data for the fission product ^{147}Nd from ^{239}Pu(n, f) as of 2011. Figure taken from Ref. [5].

is almost linear up to about 4 MeV, confirming the earlier assessment from critical assembly measurements for fission neutrons below $E_n = 2$ MeV [5,6]. The strongest overall energy dependence was seen in neutron-induced fission of ^{239}Pu. Similar positive slopes were observed in the study of ^{238}U as well. In the case of ^{235}U(n, f) the energy dependence of the FPYs shows a constant or slightly negative slope from 0.5 to 5 MeV. At higher energies ($E_n > 5$ MeV) the slope of these FPY chains turns over and becomes negative, attributed to an increased symmetric fission component.

However, the experimental results from Ref. [7] leave a gap between $E_n = 5.5$ and 14.8 MeV that is sufficiently wide that any deviation in FPY energy dependence from a monotonic increase or decrease would not be resolvable in the available literature data. Thus, the motivation of this paper is to fill in this mid-energy gap between the onset of the second-chance fission to 14.8 MeV, producing a complete, self-consistent, and high-precision FPY dataset for ^{235}U, ^{238}U, and ^{239}Pu using quasimonoenergetic neutron beams. We present a continuation to the previous dataset [7] and provide cumulative fission product yield data for the incident neutron energies: 5.5, 6.5, 7.5, 9.0, and 11 MeV. The current results includes a number of improvements to the analysis that strengthen the dataset and are described in detail below.

II. EXPERIMENTAL METHOD

The FPY measurements have been performed at the Triangle Universities Nuclear Laboratory (TUNL) using a 10 MV FN Tandem Van de Graaff accelerator. Fast quasimonoenergetic neutrons with energies of 5.5, 6.5, 7.5, 9.0, and 11.0 MeV were produced utilizing the ^{2}H$(d, n)^3$He reaction. The incident deuteron beam current was kept relatively constant at ≈ 2 μA, while the deuterium gas pressure was set to ≈ 4 atmospheres. The neutron energy spread of the beam was determined to be 100–130 keV full width at half maximum (FWHM) using the neutron time-of-flight (nTOF) technique. A cartoon schematic of our experimental setup is shown in Fig. 2. Measurements were performed using a dual-fission chamber (DFC) that was positioned 1.58 cm from the end of the 3-cm-long deuterium gas cell. The DFC, shown in Fig. 3, contains two thin ($\approx$10–100 μg/cm^2) reference foils and a thicker ($\approx$200–400 mg/cm^2) actinide activation target. The properties of the activation target and reference foils are listed in Tables I and II, respectively. The reference foils were electrodeposited onto 10 mil titanium backings and the activation targets are self-supporting. The activation target is contained in the center of the dual-fission chamber while the reference foils are held 4 mm up- and down-stream from the activation target in separate, identical, and independent fission ionization chambers (FCs), hence the name of dual-fission chamber. The activation target and reference foils are composed of the same actinide material and any differences in isotopic composition are corrected for during the analysis, see Sec. III G. We manufactured three individual DFCs and dedicated each to one of the three actinide targets so that the same activation target and reference foils were always used in the corresponding chamber. The total number of fissions in the activation target is obtained by scaling the fission counts measured by an individual chamber by the ratio of masses of the target and reference foils. A more detailed treatment concerning the DFC's can be found in Ref. [10].

Recently, the masses of the thin reference foils were remeasured using high-precision alpha spectroscopy, 2π gas counting, and γ-ray spectroscopy [8,9]. Using the High Intensity Gamma-Ray Source (HIGS) at Duke University, we irradiated each of our fission chambers with collimated, high-energy photons ($\approx$13 MeV). Since there is little divergence to the photon beam and negligible attenuation through the fission chambers, the ratio of photofission event in the reference foils for the upstream and downstream halves of the DFC must be equal to the ratio of the masses of the reference foils. It was discovered in these tests that these ratios did not match and this implied that there must have been errors in the original mass determination of these foils. A reanalysis of the original alpha spectrometry results for the ^{235}U and ^{238}U revealed geometrical considerations that were not adequately corrected for. A detailed publication detailing this remeasurement effort is forthcoming [8]. The updated masses are shown in Table II and are used in the present work.

The average neutron flux at the center of the DFC ranged from 2–6 $\times$ 10^7 n s^{-1} cm^{-2} for energies from 5.5 to 11.0 MeV, respectively. The advantage of using the DFC method, compared with other methods, such as radiochemistry, the ratio method, or mass separation, is that the fission chamber determines the total number of fissions in the target without having to explicitly know either the neutron-induced fission cross section or the neutron flux. Only the ratio of the masses of the reference foils and the activation target must be known, which greatly reduces the total uncertainty of the measurements.

Following 3–5 days of neutron activation, the activation target was removed from the center of the DFC and measured within 20–30 minutes using High-Purity Germanium (HPGe) detectors (50% relative efficiency). The targets were continuously counted for a period of 1–2 months. To the extent possible, all irradiation and counting procedures were kept the same to minimize sources of systematic errors. We fit the

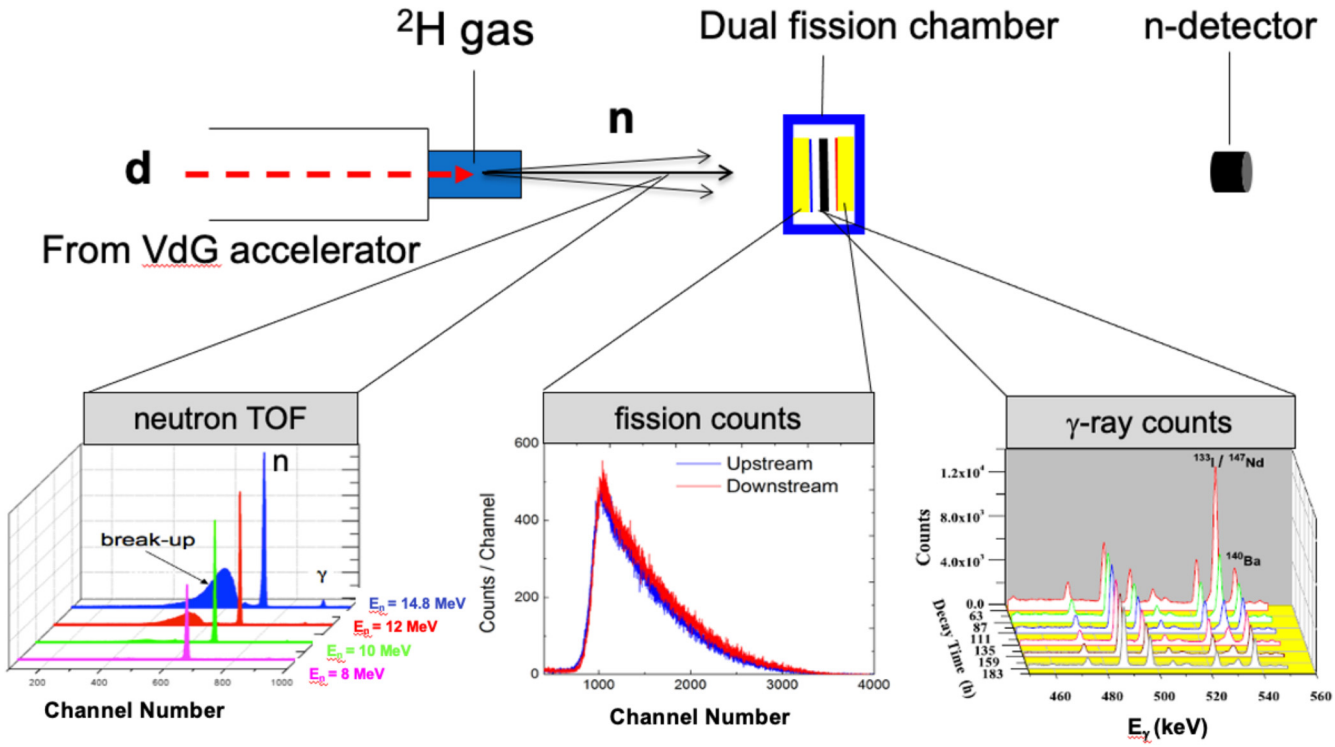

FIG. 2. Schematic of the FPY experimental setup. The bottom-left panel shows the measured nTOF spectrum, the bottom-middle panel, the DFC pulse-height spectrum, and the right panel shows the time evolution of the γ-ray spectra.

decay curve of each fission product in order to uniquely identify it and ensure the particular γ-ray line was free of interference. We developed γ-ray spectrum analysis tools based on the ROOT software to automate the analysis of sequential γ-ray spectra. These tools can automatically search for photopeaks for various radionuclide γ-ray emissions, identifying photopeak interferences with different half-lives, and solving the second-order Bateman equation to fit the activity of a daughter nucleus as a function of time. Nuclear decay data used for the analysis of the cumulative FPYs is taken from the IAEA Nuclear Data Services [11] (see Table III).

III. ANALYSIS

In the following sections we detail multiple aspects of the analysis that were undertaken to produce the fission product yields that are reported in this paper. Much of the analysis described below can also be found in Ref. [7]; however, we have made a number of improvements to the methods for computing specific corrections and we wish to detail those here. This new analysis methodology and corrections due to the changes made to the DFC reference foil masses (see Sec. II) will be applied to the existing data from Ref. [7] in a future publication.

A. Fission product yields and related uncertainties

The total fission rate in the thick activation target is calculated from each fission chamber (FC) according to

$$F_{T_n} = \frac{N_n^f}{\epsilon_n T_{\text{Live}}} \frac{m^{\text{act}}}{m_n^{\text{ref}}} C_{\text{Boost,n}} C_{\text{Flux,n}}, \tag{1}$$

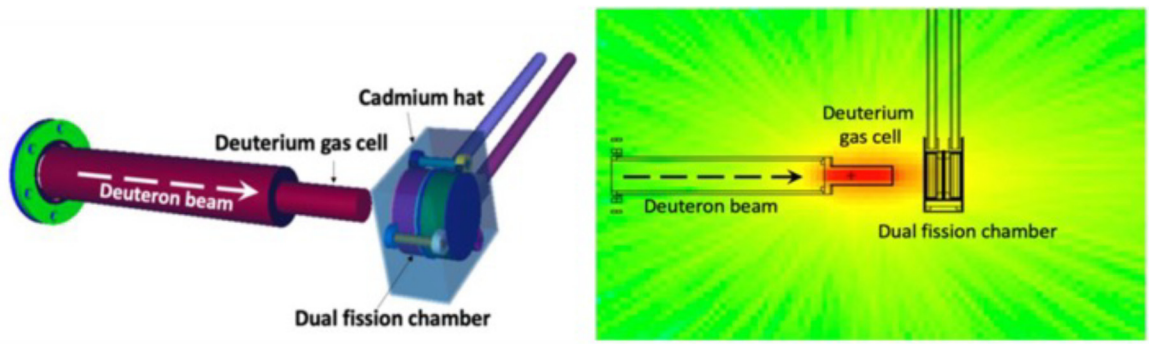

FIG. 3. The left panel shows a three-dimensional rendering of the neutron production gas cell and DFC used in this work. The right panel shows the simulated neutron flux in the vicinity of the gas cell and DFC. See text for dimensions.

TABLE I. Properties of the activation targets used for this work. The reported mass is the total gravimetric mass of the samples. See Ref. [7] for details.

Target	Diameter (mm)	Target mass (mg)	Cover material/mass (mg)	Isotopic analysis
^{235}U	12.35(5)	223.02(2)	Mylar tape	^{235}U: 93.27%, ^{234}U: 1.05%, ^{238}U: 5.68%
^{238}U	12.42(5)	441.9(6)	Mylar tape	^{238}U: 99.974%, ^{235}U: 0.026%
^{239}Pu#3	12.39(5)	233.0(2)	Ni/218.9	^{239}Pu: 98.41(40)%, ^{240}Pu: 1.58(40)%
^{239}Pu#8	12.40(5)	233.7(2)	Ni/234.5	^{241}Pu: 0.003(1)%, ^{242}Pu: 0.003(2)% ^{241}Am: 0.000572(32)% in ≈1955

where

(1) n designates the FC under consideration: $n = 1$ or 2 for downstream and upstream, respectively;
(2) N_n^f is the total number of fission counts in FC$_n$ during the irradiation time;
(3) $m^{\text{act(ref)}}$ is the mass of the activation target (reference foil);
(4) ϵ_n is the efficiency of fission chamber n;
(5) T_{Live} is the data-acquisition live time during irradiation
(6) $C_{\text{Boost,n}}$ is the correction for the kinematic boosting of fission fragments for fission chamber n;
(7) $C_{\text{Flux,n}}$ is the correction factor to convert the neutron flux at the position of reference foil n to the neutron flux at the position of the activation foil.

The fission rate in the thick target is determined by taking a weighted average of the total fissions in each half of the DFC, F_{T_1} and F_{T_2}:

$$F^T = \frac{w_1 F_{T_1} + w_2 F_{T_2}}{w_1 + w_2}, \quad w_i = \frac{1}{\sigma_i^2}, \tag{2}$$

where σ_i is the uncertainty in F_{T_i} coming from all factors in Eq. (1). After irradiation, the activation target is removed from the DFC and the induced FPY activity is measured using one of two designated HPGe detectors. The FPY for a particular fission product i is determined by the following activation equation:

$$FPY_i = \frac{\lambda_i N_i^\gamma}{F^T I_\gamma \epsilon_\gamma f(t)} \frac{C_{\text{Att}} C_{\text{Beam}} C_{\text{Iso}} C_{\text{Off}}}{C_{\text{Sum}}}, \tag{3}$$

where

(1) λ_i is the decay constant;
(2) N_i^γ is the total number of γ-ray counts in photopeak of interest;
(3) F^T is the fission rate in the activation target as determined by Eq. (2);
(4) I_γ is the intensity of the measured γ ray;
(5) ϵ_γ is the energy dependent HPGe γ-ray detection efficiency;
(6) $f(t)$ is the time factor accounting for the irradiation time t_{irr}, decay time t_d, and the measurement time t_m and is given by
$f(t) = (1 - e^{-\lambda_i t_{\text{irr}}})(1 - e^{-\lambda_i t_m}) e^{-\lambda_i t_d}$;
(7) the factors C_X correspond to corrections for photon attenuation in the target (Att), fluctuations in the beam current (Beam), isotopic impurities in the target (Iso), off-energy neutrons (Off), and coincidence summing (Sum).

TABLE II. Fission chamber reference foil masses. FC1 (FC2) is the downstream (upstream) half of the DFC. See Refs. [8,9] for details.

Foil	Chamber	Mass (μg)	Isotopic analysis
^{235}U#83	FC2	128.5(14)	99.836(2)%
^{235}U#84	FC1	129.7(14)	99.836(2)%
^{238}U#103	FC2	124.3(16)	99.9823(1)%
^{238}U#101	FC1	136.8(18)	99.9823(1)%
^{239}Pu#106	FC2	8.49(10)	99.948(8)%
^{239}Pu#107	FC1	9.26(11)	99.948(8)%

The correction factors in Eqs. (1) and (3) will be described in detail in the following sections. For a discussion of the beam-fluctuation correction, C_{Beam}, which accounts for the nonconstant nature of the neutron source with time during irradiation, see Ref. [7].

TABLE III. Nuclear data for the fission products reported in this paper, taken from Ref. [11].

Fission product	Half-life (h)	γ-ray energy (keV)	I_γ
^{91}Sr	9.65(6)	1024.3(1)	33.5(11)
^{92}Sr	2.611(17)	1383.93(5)	90(6)
^{95}Zr	1536.768(144)	756.725(12)	54.38(22)
^{97}Zr	16.749(8)	743.36(3)	93.09(16)
^{99}Mo	65.924(6)	739.500(17)	12.2(2)
^{103}Ru	941.928(312)	497.085(10)	91.0(12)
^{105}Ru	4.439(11)	724.211(10)	47.8(6)
^{127}Sb	92.4(1.2)	685.7(5)	36.8(20)
^{131}I	192.6048(144)	364.489(5)	81.5(8)
^{132}Te	76.896(312)	228.16(6)	88(4)
^{133}I	20.83(8)	529.872(3)	87.0(23)
^{135}I	6.58(3)	1260.409(17)	28.7(9)
^{135}Xe	9.14(2)	249.794(15)	90(3)
^{136}Cs	312.24(1.20)	1048.073(20)	80(3)
^{140}Ba	306.024(96)	537.261(9)	24.39(22)
^{143}Ce	33.039(6)	293.266(2)	42.8(4)
^{144}Ce	6837.84(1.20)	133.515(2)	11.09(19)
^{147}Nd	264.72(72)	531.012(18)	13.11(13)

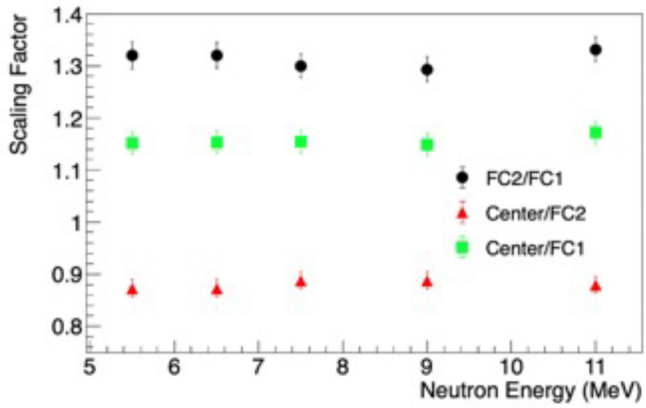

FIG. 4. Simulated neutron flux ratios between the downstream (FC1), upstream (FC2), and center (activation) foils for the ^{238}U DFC.

B. Fission chamber neutron flux determination (C_{Flux})

Because the DFC is positioned near the deuterium gas cell, each of the three foils subtends a different solid angle relative to the center of the neutron source. This results in slightly different neutron energy and flux distributions at the position of each foil. To account for these effects, we developed an MCNP [12] simulation to determine the scaling factor C_{Flux} that converts the neutron flux at the position of each thin reference foil to the flux at the position of the thick target in the DFC. Our MCNP model included a detailed description of the deuterium gas cell with the Havar foil separating the deuterium gas from the vacuum and the DFC, as shown in the left panel of Fig. 3. To accurately account for the neutron energy and angular distributions from the $^{2}\mathrm{H}(d,n)^{3}\mathrm{He}$ reactions, we started our simulation with an incident deuteron beam impinging onto the 4-atmosphere deuterium gas cell. We assumed a 4 mm × 4 mm cross-sectional area based on a postirradiation measurement of the beam spot on the Havar foil. The energy loss and straggling in the Havar foil, the opening angle and the neutron angular distribution at each incident energy, and the effect of the attenuation of neutrons through the DFC have been explicitly considered in the simulation. The contribution from the room-return neutrons was found to be negligible in Ref. [10], and hence not included in the MCNP simulation. However, to ensure there is no contribution from room-return neutrons the fission chambers are covered with a Cd "hat" during the irradiations that can be seen in the left panel of Fig. 3. An example neutron density distribution produced from a $^{2}\mathrm{H}(d,n)^{3}\mathrm{He}$ reaction with $E_n = 6.5$ MeV is shown in the right panel of Fig. 3.

Figure 4 displays the scaling factors C_{Flux} between the neutron flux in the thick ^{238}U activation target and the upstream (downstream) FC2 (FC1) reference foils for different incident neutron energies. For all these calculations, the DFC was positioned 1.58 cm from the face of the gas cell. The error bars represent the statistical uncertainty (<1.5%) based on the random samplings of the individual physical processes. Proper alignment of the DFC relative to the gas cell was made using a laser and an optical telescope. However, a 1.5% systematic error (not shown in Fig. 4) due to an uncertainty of 1 mm in the distance between the gas cell and DFC is estimated using MCNP. As a check of the validity of the MCNP results, the simulated ratio of the flux in the two chambers FC2 (FC1) upstream (downstream) scaled by the foil masses was compared with the ratio of measured fission events in the two chambers. The agreement is generally good, with a variation between in the simulation and experiment of 1.0%–3.5%. One exception is at 11 MeV, where the difference is 6.6%. This is likely due to the presence of off-energy neutrons in the experiment that were not included in the simulation (discussed below).

C. Kinematic boosting of fission fragments (ϵ_{FC}, C_{Boost})

A GEANT4 [13] model was developed to simulate the fission-fragment detection efficiency of the DFC. The simulation accounts for two phenomena that impact the detection efficiency. First, the fission fragments must escape the actinide layer where they are generated and then deposit energy into the active gas region via ionization. Second, the incident neutron which induces the fission event imparts momentum to the fissioning nucleus. This kinematic boost has opposite effects in both chambers; the upstream chamber (FC2) sees a decrease in efficiency as the fragments are boosted away from the ionization gas and into the titanium backing, while the downstream chamber (FC1) sees an increase in efficiency as the fragments are boosted into the gas region.

The GEANT4 model includes the FC foil titanium backing, actinide deposit layer, and P-10 (CH_4 10%; Ar 90%) gas region. In a single fission event, a pair of fission fragments are emitted from a random location in the actinide layer. The pair of fragments are given the appropriate kinematic boost for the incident neutron beam energy and chamber orientation (i.e., upstream or downstream). The fission event is considered detected if one or both of the fission fragments deposit more than 10 MeV into the ionization chamber gas. The simulated FC pulse-height spectra match the experimental spectra, so the simulation threshold was chosen to match the experimental one.

The pairs of fission fragments were generated using the event-by-event fission modeling code FREYA [14]. Fission-fragment pairs were generated for each actinide target at every incident neutron energy using FREYA v.2.0.5 with default parameter settings. Each fragment in a correlated pair had the following information: mass, nuclear charge, momentum direction, and kinetic energy. The simulated FC detection efficiencies are plotted in Fig. 5. As a general trend, increasing the neutron beam energy (and thus kinematic boost) increases the disparity between the upstream and downstream FC efficiencies. Additionally, the ^{239}Pu FCs have greater detection efficiency than the ^{235}U and ^{238}U because the ^{239}Pu actinide deposits are about an order of magnitude thinner. Simulations are consistent with efficiency measurements performed with ^{252}Cf in Ref. [10]. According to Ref. [15] the effect of the fragment anisotropy on FC efficiency is much smaller than angular-momentum effect (<1% for neutrons below 15 MeV) and was not considered in the present simulations.

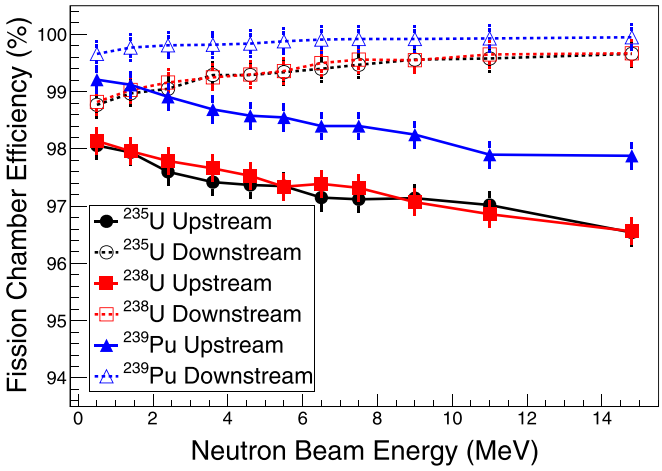

FIG. 5. Fission event detection efficiency as a function of incident neutron energy for the upstream and downstream FCs loaded with all three actinide targets. The ^{239}Pu targets have less material for the fragments to pass through, and thus have an overall higher detection efficiency compared with the uranium foils.

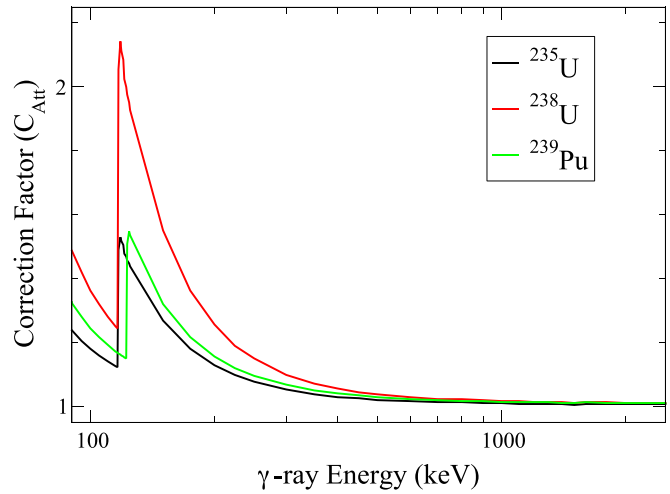

FIG. 6. The correction factor C_{Att} accounts for γ-ray self-absorption and geometrical differences from the detector calibration source as a function of γ-ray energy for ^{235}U (black), ^{238}U (red), and ^{239}Pu (green).

D. HPGe detector efficiency (ϵ_γ)

Following neutron irradiation, the activation target was removed from its fission chamber and the induced activity was measured by γ-ray spectroscopy using one of two designated coaxial HPGe detectors. Each detector is housed within a custom lead shield in the TUNL low-background counting facility. Energy and efficiency calibrations were performed using a multinuclide point source from Eckert and Zeigler covering the range between 60 and 1900 keV.

Affixed to the end cap of each detector is an acrylic sample position shelf system with predefined sample counting positions given from the face of the detector at distances of 2.5, 5, 7.5, 10, 15, 20, and 25 cm. We also used clear acrylic cylindrical sample holders that mount rigidly into the shelf system such that the center of the sample holder is at the specified counting distance and co-axial with the detector. To accommodate the different thickness of the activation targets ($\approx$1 mm) and calibration sample (5 mm) in the same holder, cylindrical spacers of different thickness were used to center the samples in the acrylic holder. Because the holder was clear, the positioning could be verified by eye. Each counting position is well calibrated using the multinuclide source at close distances and in combination with other source at further distances (^{133}Ba, ^{56}Co, etc.). Due to the inherent activity of the actinide targets, we utilized Cd attenuators on the face of each detector to reduce the HPGe detector dead-times during acquisition. For ^{235,238}U this was an 0.5-mm-thick sheet and for ^{239}Pu we used a 2 mm Cd sheet. Detector calibrations were performed with the attenuators in place.

To balance counting statistics and coincidence summing effects, all targets were counted at 5 cm from the face of the detector. For consistency, the ^{239}Pu sample was only counted on HPGe detector #1 and the two uranium targets were counted on HPGe detector #2. The consequence of which is that only two out of the three targets could be measured in any single irradiation campaign. Both HPGe detectors were modeled using MCNP [12] according to the manufacturer's specification sheet. The MCNP geometry is comprised of the HPGe detector, the multinuclide source, the acrylic target holder, and the lead housing. To optimize the MCNP calculation, the front and side dead layers of the germanium crystal have been adjusted to reproduce closely the experimental efficiency measurements at 5 cm without the cadmium attenuators in place. The same MCNP geometry was then used to simulate the detector efficiency at various source distances and cadmium thicknesses.

As described below in Sec. III F, MCNP was used to perform coincidence summing corrections for several of the γ-ray lines within the calibration source. Since the calibration source is designed to have radioisotopes which emit γ rays with little or no summing, the majority of the lines required no summing correction, and only a few were corrected up to 5%. Overall, there was very good agreement between the modeled MCNP detector efficiency and the measured efficiency with less than $\pm$5% difference over the full energy range of 60–1900 keV. However, the MCNP model was only used to make coincidence summing corrections to the measured efficiency data points. Those experimental values were fit with a five-parameter empirical function from Refs. [16,17] that is optimized for the energy range of 63–3054 keV.

To account for the possibility that errors might occur when positioning the activated target or calibration source within the sample holders, the measured efficiency curve was scaled by a "self-normalization" factor determined for each sample measurement. We did this using our targets as calibration sources with their well-known masses and natural γ-ray lines. Then we were able to determine small scaling factors to the measured efficiency curve to ensure it reproduced the known activity of the natural lines within our targets. Multiple γ-ray lines from each target were used and, accounting for self-absorption, all agreed very well. The self-normalization correction was generally less than 5%.

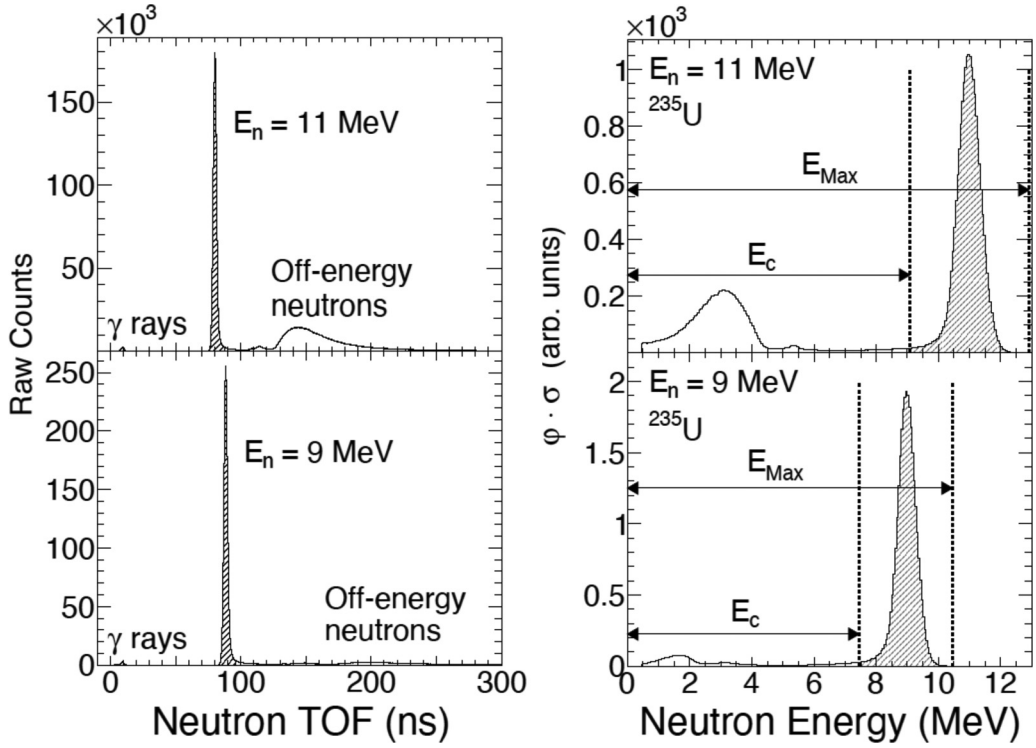

FIG. 7. (left panel) *n*TOF spectrum for 11 MeV (top) and 9 MeV (bottom) as measured by a liquid scintillator detector for the ^{2}H$(d, n)^{3}$He reaction. Plots are unnormalized. See text for description of features in the spectra. (right panel) Plot of the *n*TOF spectra from the left panel converted to energy and folded with the fission cross section [22] at 9 MeV (bottom) and 11 MeV (top). The spectrum is divided into regions of off-energy neutrons below E_C and monoenergetic neutrons between E_C and E_{Max} (shaded region in the right panel).

E. Attenuation correction (C_{Att})

Due to matter interactions, γ rays emitted throughout the volume of the target experience self-absorption before reaching the detector. Unless a detector calibration is carried out using sources with the same volume and material as the target, self-absorption corrections are needed to establish the absolute γ-ray emission rates of any fission products and thereby determine their yield. This correction becomes significant for lower γ-ray energies, larger sample volumes and densities, and larger solid angles. In previous work, we used the analytic expression for γ-ray attenuation and self-absorption through the activation target thickness [7]. However, the path length that the photons take through the target varies due to the angle at which they are emitted and the γ rays being emitted throughout the actinide volume. This effect was corrected for analytically in our previous results, however, in this work we have employed an MCNP simulation to determine the correction factor. The simulated attenuation results agreed with our previous analytical results within the involved uncertainties. Calculations have been made for the geometrical and material differences between the multinuclide calibration source and the activation targets (see Fig. 6).

F. Coincidence summing (C_{Sum})

The detection efficiency of a γ ray emitted as part of a nuclear decay can be influenced by the emission of other γ rays during that decay. In β decay, the process by which most fission products decay, a γ ray of interest is typically part of a larger cascade of γ rays emitted in a sufficiently fast sequence so as to be treated as a single event by the HPGe. Even if the γ ray of interest deposits its full energy into the HPGe, one or more coincident γ rays in the cascade may deposit some of their energy in the detector, causing the total detected energy to fall outside the photopeak area and into the continuum. This effect, referred to as summing out, reduces the apparent HPGe detection efficiency for a γ ray in a particular nuclear decay. Alternatively, there may be two γ rays in the cascade whose combined energy equals that of the γ ray of interest; if both of those γ rays deposit their full energy into the HPGe in coincidence, a false count will be added to the photopeak of interest. This effect is referred to as summing in, and has the effect of increasing the apparent HPGe detection efficiency for a γ ray in a particular nuclear decay. The coincidence summing correction factor accounts for both of these phenomena.

In general, summing out has a larger impact than summing in, so the summing correction factor (which multiplies the

TABLE IV. Parameters and corrections for off-energy neutrons at a measurement energy of 9 MeV.

Actinide	$\mathbf{R_{BT}}$	$\bar{E}$ (MeV)	$\bar{E}_B$ (MeV)	C_{Off} for ^{147}Nd
^{235}U	0.100 ± 0.001	8.36 ± 0.01	2.90 ± 0.02	0.972 ± 0.003
^{238}U	0.064 ± 0.001	8.63 ± 0.01	3.81 ± 0.01	0.985 ± 0.002
^{239}Pu	0.116 ± 0.001	8.25 ± 0.01	2.86 ± 0.02	0.969 ± 0.006

TABLE V. Parameters and corrections for off-energy neutrons at a measurement energy of 11 MeV.

Actinide	$\mathbf{R_{BT}}$	$\bar{E}$ (MeV)	$\bar{E}_B$ (MeV)	C_{Off} for ^{147}Nd
^{235}U	0.350 ± 0.001	8.25 ± 0.101	3.20 ± 0.01	0.872 ± 0.016
^{238}U	0.280 ± 0.001	8.88 ± 0.01	3.53 ± 0.01	0.938 ± 0.013
^{239}Pu	0.387 ± 0.001	7.94 ± 0.01	3.17 ± 0.01	0.863 ± 0.027

HPGe detection efficiency) is less than 1. It should be noted, however, that there are rare cases where the summing-in effect is large and the overall summing correction is greater than 1. One example is the 1678.03 keV γ ray from ^{135}I, which has a coincidence summing correction of 1.024 for the ^{238}U target in the present counting geometry.

We developed the C++ code CADETS (CAscade DETection Summing) for calculating the summing correction factor, based on the prescription in Ref. [18] and implementation of Ref. [19]. CADETS reads the level energies, β-decay branching ratios, and γ-ray emission probabilities for each level in the decay daughter nucleus from ENSDF decay-data files [20]. It then recursively searches for all possible decay cascades that include the γ ray of interest in order to calculate the summing-out correction. For the summing-in correction, the code recursively searches for all decay paths that include two γ rays whose energy sums to within 1 keV of the γ ray of interest. Of course, it is possible for three γ rays to sum to the energy of the γ ray of interest, but the probability of detecting all three γ rays in coincidence becomes vanishingly small.

TABLE VI. ^{235}U fission yield data. Total uncertainties at 1σ are given and produced from a sum in quadrature of individual terms assuming no correlations.

Source of uncertainties	Magnitude (%)
Photopeak area*	0.2–1
FC counts*	<0.2
Target masses	<0.5
FC reference foil masses	0.9–1.2
FC efficiency*	0.2
Neutron flux at target*	1.3
Beam fluctuation corr.*	<0.05
Off-energy neutron corr.*	0.1–2.7
Room-return background	$\ll$1
Half-lives	$\ll$1
Absolute γ-ray emission prob.	0.2–6.7
HPGe detector efficiency	0.8–2.0
Self-normalization stats.*	0.3
Self-normalization corr.	1
True coincidence summing	<1
Random summing	<0.2
Isotopic corrections	0.2
Irradiation times*	$\ll$1
Decay times*	$\ll$1
Counting times*	$\ll$1
Total	2.4–7.9
*Reduced (see text)	1.4–3.2

In addition to the nuclear decay information, the other inputs required to calculate the summing correction are the HPGe photopeak efficiency and total detection efficiency. The photopeak efficiency is defined as the probability that a γ ray of a given energy deposits its full energy into the detector (i.e., it would fall in the photopeak area). The total detection efficiency is the probability that a γ ray of a given energy deposits any of its energy; the γ ray may be fully absorbed in the HPGe or it may scatter out of the detector, scatter prior to hitting the detector, emit an annihilation γ ray that is not absorbed, etc. For these calculations, both the photopeak and total detection efficiencies were calculated with the calibrated MCNP models of the HPGe detectors described previously. A direct measurement of the summing correction for the 739.5 keV γ ray from ^{99}Mowas performed using an irradiated natural molybdenum foil. The foil was assayed at a large source-to-detector distance where there is no summing effect, and then at the standard counting position. This direct measurement of the summing showed good agreement with the MCNP simulation.

G. Target isotopic corrections (C_{Iso})

The ^{235}U and ^{239}Pu activation targets have impurities from other fissionable isotopes (see Table I). These impurities contribute both to the total number of fissions in the thick target and the γ rays detected from a particular fission product. The contributions of the impurities must be subtracted to determine the FPYs from only ^{235}U or ^{239}Pu. For a specific fission product i from actinide target A, the FPY is calculated according to

$$FPY_{A,i} = \frac{\lambda_i N_i^{\gamma}}{\phi N_A \sigma_A I_{\gamma} \epsilon_{\gamma} f(t)} - \sum_{j, j \neq A} FPY_j \frac{N_j \sigma_j}{N_A \sigma_A}, \qquad (4)$$

where N_A and σ_A are the number of atoms and fission cross section for actinide A (^{235}U, ^{238}U, or ^{239}Pu). From Eq. (3) we see that C_{Iso} is defined as a multiplicative factor and therefore, we can rearrange Eq. (4) and define our isotopic correction factor as

$$C_{\text{Iso}} = 1 - \sum_{j, j \neq A} FPY_j \frac{\phi N_j \sigma_j I_{\gamma} \epsilon_{\gamma} f(t)}{\lambda_i N_i^{\gamma}}. \qquad (5)$$

From Eq. (5), it is clear that the fission product yields from the impurities must be known at the energy of interest. For the ^{235}U target, the main impurities are ^{234}U and ^{238}U. For the ^{239}Pu foil, the impurity is primarily ^{240}Pu [7]. For ^{235}U, we utilize the FPY values that we have measured for ^{238}U. However, since ^{234}U and ^{240}Pu were not measured in this work, FPYs from the phenomenological fission code GEF are used [21]. Fission cross sections were taken from the ENDF/B-VIII.0 library [22].

H. Off-energy neutron corrections

The main goal of this work was to study the energy dependence of the FPYs in the second-chance fission region. These FPYs were measured at specific energies using quasimonoenergetic neutrons. However, when using the ^{2}H$(d, n)^3$He reaction to produce neutrons above $\approx$5.5 MeV, a continuum

TABLE VII. Cumulative fission product yield results for ^{239}Pu(n, f).

	Incident neutron energy (MeV)				
Fission product	5.5 ± 0.13 FPY $\pm \sigma_T(\sigma_R)$	6.5 ± 0.13 FPY $\pm \sigma_T(\sigma_R)$	7.5 ± 0.30 FPY $\pm \sigma_T(\sigma_R)$	9.0 ± 0.12 FPY $\pm \sigma_T(\sigma_R)$	11.0 ± 0.11 FPY $\pm \sigma_T(\sigma_R)$
^{91}Sr	3.32 ± 0.13(0.06)	3.24 ± 0.12(0.07)	3.23 ± 0.12(0.06)	3.12 ± 0.12(0.06)	3.09 ± 0.13(0.07)
^{92}Sr	3.48 ± 0.24(0.06)	3.46 ± 0.24(0.06)	3.44 ± 0.24(0.07)	3.16 ± 0.22(0.06)	3.25 ± 0.28(0.09)
^{95}Zr	5.11 ± 0.09(0.06)	5.03 ± 0.07(0.06)	5.08 ± 0.09(0.08)	5.14 ± 0.09(0.08)	4.85 ± 0.11(0.10)
^{97}Zr	5.96 ± 0.10(0.07)	5.79 ± 0.08(0.07)	5.73 ± 0.09(0.09)	5.57 ± 0.09(0.09)	5.63 ± 0.12(0.11)
^{99}Mo	5.98 ± 0.14(0.08)	6.24 ± 0.12(0.11)	6.23 ± 0.13(0.12)	5.96 ± 0.13(0.12)	5.64 ± 0.16(0.11)
^{103}Ru	6.25 ± 0.13(0.11)	6.08 ± 0.11(0.10)	6.04 ± 0.13(0.11)	5.94 ± 0.13(0.11)	5.90 ± 0.16(0.12)
^{105}Ru	5.53 ± 0.13(0.07)	5.28 ± 0.20(0.10)	5.24 ± 0.20(0.11)	5.21 ± 0.20(0.10)	4.93 ± 0.22(0.12)
^{127}Sb	1.24 ± 0.07(0.02)	1.62 ± 0.09(0.04)		1.79 ± 0.11(0.04)	
^{131}I	3.63 ± 0.18(0.17)	4.75 ± 0.08(0.08)	4.84 ± 0.09(0.09)	5.03 ± 0.10(0.10)	5.11 ± 0.11(0.10)
^{132}Te	4.04 ± 0.20(0.05)	3.84 ± 0.14(0.07)	3.80 ± 0.15(0.08)	3.54 ± 0.14(0.07)	3.54 ± 0.15(0.07)
^{133}I	6.40 ± 0.20(0.07)	6.50 ± 0.19(0.11)	6.51 ± 0.20(0.12)	6.16 ± 0.20(0.12)	5.86 ± 0.22(0.12)
^{135}I	5.32 ± 0.20(0.08)	4.93 ± 0.17(0.09)	4.94 ± 0.18(0.10)	4.46 ± 0.19(0.10)	4.23 ± 0.21(0.04)
^{135}Xe	6.56 ± 0.25(0.08)	6.68 ± 0.13(0.13)	6.44 ± 0.11(0.11)	5.95 ± 0.12(0.11)	5.69 ± 0.14(0.11)
^{136}Cs	–	0.305 ± 0.004(0.005)	0.48 ± 0.02(0.009)	0.51 ± 0.009(0.01)	0.54 ± 0.024(0.011)
^{140}Ba	4.99 ± 0.09(0.06)	4.84 ± 0.08(0.07)	4.79 ± 0.10(0.10)	4.64 ± 0.09(0.09)	4.34 ± 0.11(0.09)
^{143}Ce	3.50 ± 0.07(0.04)	3.41 ± 0.07(0.06)	3.48 ± 0.07(0.07)	3.31 ± 0.07(0.06)	2.84 ± 0.09(0.06)
^{144}Ce	–	–	–	–	–
^{147}Nd	2.43 ± 0.05(0.04)	1.97 ± 0.04(0.04)	1.86 ± 0.04(0.04)	1.72 ± 0.04(0.04)	1.64 ± 0.06(0.03)

of neutrons is produced by deuteron breakup reactions on the tantalum beam stop and above ≈7.7 MeV by breakup on the deuterium gas. This continuum is well separated from the monoenergetic neutron peak by 5.5 MeV but will still induce fissions in the targets. Also, small quantities of neutrons can be produced at specific energies by (d, n) reactions on contaminants in the beam line, such as carbon from vacuum pump oil.

The neutron energy spectrum was measured using the *n*TOF technique. The incident deuteron beam was pulsed and neutrons were measured with a cylindrical BC501A liquid scintillator detector (diameter = 3.81 cm, height = 3.81 cm) or a heavily shielded NE213 liquid scintillator (diameter = 4.44 cm, height = 5.04 cm) placed in the neutron beam 3–5 m downstream of the DFC. Spectra from such measurements are shown in the left panel of Fig. 7. The different

TABLE VIII. Cumulative fission product yield results for ^{235}U(n, f).

	Incident neutron energy (MeV)				
Fission product	5.5 ± 0.13 FPY $\pm \sigma_T(\sigma_R)$	6.5 ± 0.13 FPY $\pm \sigma_T(\sigma_R)$	7.5 ± 0.30 FPY $\pm \sigma_T(\sigma_R)$	9.0 ± 0.12 FPY $\pm \sigma_T(\sigma_R)$	11.0 ± 0.11 FPY $\pm \sigma_T(\sigma_R)$
^{91}Sr	5.58 ± 0.21(0.08)	5.76 ± 0.23(0.11)	5.63 ± 0.22(0.11)	5.45 ± 0.22(0.11)	5.03 ± 0.21(0.10)
^{92}Sr	5.52 ± 0.38(0.07)	5.12 ± 0.38(0.11)	5.82 ± 0.42(0.12)	5.25 ± 0.39(0.12)	4.89 ± 0.36(0.09)
^{95}Zr	6.23 ± 0.11(0.08)	6.10 ± 0.11(0.10)	5.99 ± 0.12(0.12)	5.79 ± 0.11(0.10)	5.43 ± 0.13(0.10)
^{97}Zr	6.56 ± 0.11(0.08)	5.93 ± 0.10(0.08)	6.06 ± 0.11(0.11)	5.85 ± 0.11(0.10)	5.57 ± 0.12(0.10)
^{99}Mo	6.37 ± 0.16(0.08)	6.00 ± 0.14(0.12)	5.87 ± 0.13(0.11)	5.51 ± 0.13(0.11)	5.20 ± 0.14(0.09)
^{103}Ru	3.82 ± 0.08(0.05)	3.43 ± 0.08(0.07)	3.13 ± 0.07(0.06)	3.07 ± 0.07(0.06)	2.88 ± 0.08(0.05)
^{105}Ru	2.00 ± 0.05(0.03)	2.15 ± 0.09(0.06)	1.89 ± 0.09(0.06)	2.21 ± 0.09(0.06)	2.24 ± 0.10(0.06)
^{127}Sb	0.98 ± 0.06(0.01)	0.98 ± 0.06(0.02)	1.05 ± 0.06(0.03)	1.17 ± 0.07(0.03)	1.54 ± 0.09(0.04)
^{131}I	4.06 ± 0.09(0.05)	4.18 ± 0.09(0.08)	4.19 ± 0.09(0.08)	4.24 ± 0.09(0.07)	4.46 ± 0.11(0.07)
^{132}Te	5.32 ± 0.26(0.06)	5.06 ± 0.20(0.10)	4.87 ± 0.20(0.09)	4.60 ± 0.19(0.10)	4.14 ± 0.18(0.08)
^{133}I	6.87 ± 0.22(0.08)	6.45 ± 0.21(0.13)	6.55 ± 0.21(0.12)	6.11 ± 0.20(0.12)	5.57 ± 0.20(0.10)
^{135}I	6.36 ± 0.23(0.08)	5.65 ± 0.21(0.11)	5.81 ± 0.21(0.11)	5.40 ± 0.20(0.09)	4.89 ± 0.18(0.09)
^{135}Xe	6.92 ± 0.27(0.09)	6.34 ± 0.13(0.13)	6.43 ± 0.13(0.12)	6.05 ± 0.13(0.12)	5.51 ± 0.14(0.10)
^{136}Cs		0.039 ± 0.002(0.002)	0.074 ± 0.004(0.003)	0.099 ± 0.005(0.003)	0.100 ± 0.006(0.003)
^{140}Ba	5.52 ± 0.11(0.07)	5.66 ± 0.11(0.10)	5.33 ± 0.11(0.10)	5.18 ± 0.11(0.10)	4.73 ± 0.12(0.09)
^{143}Ce	4.72 ± 0.10(0.06)	4.72 ± 0.11(0.09)	4.77 ± 0.10(0.09)	4.43 ± 0.10(0.09)	3.76 ± 0.10(0.07)
^{144}Ce		3.83 ± 0.98(0.98)	3.90 ± 0.72(0.72)	3.53 ± 0.52(0.51)	3.31 ± 0.45(0.17)
^{147}Nd	2.26 ± 0.05(0.03)	2.08 ± 0.04(0.04)	2.06 ± 0.05(0.04)	1.85 ± 0.04(0.04)	1.73 ± 0.05(0.03)

TABLE IX. Cumulative fission product yield results for ^{238}U(n, f).

	Incident neutron energy (MeV)				
Fission product	5.5 ± 0.13 FPY $\pm \sigma_T(\sigma_R)$	6.5 ± 0.13 FPY $\pm \sigma_T(\sigma_R)$	7.5 ± 0.30 FPY $\pm \sigma_T(\sigma_R)$	9.0 ± 0.12 FPY $\pm \sigma_T(\sigma_R)$	11.0 ± 0.11 FPY $\pm \sigma_T(\sigma_R)$
^{91}Sr	$4.25 \pm 0.17(0.07)$	$4.12 \pm 0.16(0.10)$	$4.13 \pm 0.16(0.08)$	$4.13 \pm 0.16(0.07)$	$3.82 \pm 0.15(0.06)$
^{92}Sr	$4.19 \pm 0.30(0.07)$	$4.34 \pm 0.30(0.09)$	$4.13 \pm 0.29(0.08)$	$4.29 \pm 0.30(0.08)$	$3.84 \pm 0.27(0.06)$
^{95}Zr	$5.19 \pm 0.10(0.07)$	$5.24 \pm 0.14(0.13)$	$5.17 \pm 0.09(0.08)$	$5.11 \pm 0.09(0.08)$	$4.91 \pm 0.10(0.08)$
^{97}Zr	$5.79 \pm 0.11(0.08)$	$6.01 \pm 0.12(0.10)$	$5.48 \pm 0.09(0.09)$	$5.41 \pm 0.09(0.09)$	$5.22 \pm 0.10(0.08)$
^{99}Mo	$6.04 \pm 0.15(0.09)$	$5.90 \pm 0.34(0.31)$	$6.07 \pm 0.13(0.10)$	$5.97 \pm 0.13(0.10)$	$5.73 \pm 0.15(0.09)$
^{103}Ru	$5.88 \pm 0.13(0.08)$	$5.48 \pm 0.13(0.10)$	$5.35 \pm 0.11(0.09)$	$5.26 \pm 0.11(0.09)$	$4.62 \pm 0.12(0.07)$
^{105}Ru	$4.01 \pm 0.10(0.07)$	$3.78 \pm 0.15(0.07)$	$3.62 \pm 0.15(0.08)$	$3.33 \pm 0.14(0.08)$	$2.72 \pm 0.12(0.05)$
^{127}Sb	$0.39 \pm 0.02(0.01)$	$0.42 \pm 0.03(0.02)$	$0.46 \pm 0.03(0.01)$	$0.68 \pm 0.04(0.02)$	$0.77 \pm 0.06(0.02)$
^{131}I	$3.30 \pm 0.07(0.05)$	$3.54 \pm 0.08(0.06)$	$3.50 \pm 0.07(0.06)$	$3.79 \pm 0.08(0.06)$	$3.82 \pm 0.09(0.06)$
^{132}Te	$4.84 \pm 0.24(0.06)$	$5.15 \pm 0.21(0.09)$	$5.11 \pm 0.21(0.11)$	$5.01 \pm 0.21(0.10)$	$4.64 \pm 0.20(0.08)$
^{133}I	$6.48 \pm 0.21(0.08)$	$6.80 \pm 0.23(0.12)$	$6.61 \pm 0.21(0.11)$	$6.61 \pm 0.21(0.11)$	$5.89 \pm 0.20(0.10)$
^{135}I	$6.54 \pm 0.11(0.03)$	$6.66 \pm 0.24(0.11)$	$6.48 \pm 0.23(0.11)$	$6.25 \pm 0.23(0.11)$	$5.38 \pm 0.21(0.09)$
^{135}Xe	$6.37 \pm 0.25(0.09)$	$6.72 \pm 0.58(0.14)$	$6.55 \pm 0.13(0.11)$	$6.63 \pm 0.13(0.11)$	$5.23 \pm 0.13(0.08)$
^{136}Cs		$0.012 \pm 0.005(0.002)$	$0.007 \pm 0.001(0.001)$	$0.006 \pm 9.106 \times 10^{-4}$ (8.864×10^{-4})	$0.004 \pm 5.571 \times 10^{-4}$ (5.388×10^{-4})
^{140}Ba	$5.43 \pm 0.11(0.07)$	$5.41 \pm 0.14(0.13)$	$5.36 \pm 0.10(0.09)$	$5.32 \pm 0.10(0.09)$	$4.82 \pm 0.10(0.08)$
^{143}Ce	$4.50 \pm 0.10(0.06)$	$4.44 \pm 0.11(0.07)$	$4.32 \pm 0.09(0.07)$	$4.35 \pm 0.09(0.07)$	$3.97 \pm 0.10(0.06)$
^{144}Ce					$3.44 \pm 0.19(0.18)$
^{147}Nd	$2.58 \pm 0.06(0.04)$	$2.38 \pm 0.14(0.14)$	$2.35 \pm 0.05(0.04)$	$2.32 \pm 0.05(0.04)$	$2.14 \pm 0.05(0.04)$

structures seen to the right of the large monoenergetic peak from the ^{2}H$(d, n)^3$He reaction come from deuteron breakup and reactions on contaminants in the beam line, as mentioned previously. The *n*TOF spectrum can be converted to an energy spectrum and folded with the neutron detector efficiency [23], as shown in the right panel of Fig. 7. The resulting neutron spectrum can then be folded with the fission cross section [22] for the isotope of interest to determine the correction. The neutron energy spectrum was measured down to ≈0.5 MeV, limited by the 400 ns timing of the beam pulsing.

A correction must be made to remove the contributions of the off-energy neutrons to both the observed FPY and the number of fission events detected in the DFC. We define a cutoff energy E_c such that above this energy are our monoenergetic neutrons and below there are breakup or other off-energy neutrons. The contributions due to neutrons below E_c are subtracted from the observed FPY according to

$$FPY_i = \frac{\lambda_i N_i^\gamma}{\bar{\imath} f(t) F_T \int_{E_c}^{E_{\rm Max}} \phi(E)\sigma(E)dE} \times \left(1 - \frac{FPY_i(\bar{E}_B)\int_0^{E_c}\phi(E)\sigma(E)dE}{FPY_i(\bar{E})\int_0^{E_{\rm Max}}\phi(E)\sigma(E)dE}\right), \quad (6)$$

where we have defined the average neutron energy and average breakup neutron energy as

$$\bar{E}(\bar{E}_B) = \frac{\int_0^{E_{\rm Max}(E_c)} E\phi(E)\sigma(E)dE}{\int_0^{E_{\rm Max}(E_c)}\phi(E)\sigma(E)dE}. \quad (7)$$

In deriving Eq. (6), to simplify the calculation, we have taken $FPY(E)$ outside of the integrals and replaced it with its average under the assumption that it varies slowly with energy. There is a similar correction necessary for the fission chambers:

$$F_{T_i}' = F_i^T\left(1 - \frac{\int_0^{E_c}\phi(E)\sigma(E)dE}{\int_0^{E_{\rm Max}}\phi(E)\sigma(E)dE}\right). \quad (8)$$

Since the neutron spectrum is the same for all FPYs for a given actinide, we define the ratio of breakup-to-total neutrons in the spectrum as

$$R_{\rm BT} = \frac{\int_0^{E_c}\phi(E)\sigma(E)dE}{\int_0^{E_{\rm Max}}\phi(E)\sigma(E)dE}. \quad (9)$$

Combining Eqs. (6) to (9), the total correction factor is

$$C_{\rm Off} = (1 - R_{\rm BT})^{-1}\left(1 - R_{\rm BT}\frac{FPY_i(\bar{E}_B)}{FPY_i(\bar{E})}\right). \quad (10)$$

Fission cross sections were taken from the ENDF/B-VIII.0 library [22], and the FPY values at lower energies were taken from those available in this work and previously published results [7]. To illustrate the correction factor, the values of various parameters in Eq. (10) are given in Tables IV and V for the 9 and 11 MeV incident neutron energies, respectively.

In addition to the off-energy (by deuterium breakup) neutrons, low-energy background (the so-called room return) neutrons can contribute to the fission events of thermally fissile isotopes ^{235}U and ^{239}Pu that are not measured by the neutron TOF approach described above. To obtain quantitative data on these low-energy neutrons we have recorded TOF spectra using pulsed beam (2.5 MHz repetition rate with pulse width of 2.5 ns) at different neutron energies using ^{235}U and ^{239}Pu FCs. Based on these TOF and activation foil measurements [10] the room-return neutron contribution is

negligible (i.e., <1%) and corrections are required only for the off-energy neutrons.

IV. UNCERTAINTIES

A summary of the various sources of uncertainty and their magnitudes are presented in Table VI. All uncertainties were carefully considered, and in cases where the uncertainty was unknown (e.g., simulated values), reasonable estimates were made. The total uncertainty is determined by summing in quadrature all source of uncertainties listed in Table VI. The reduced uncertainty excludes those factors that are common to all energy measurements and therefore includes only statistical uncertainties, the HPGe efficiency self-normalization, the conversion of the neutron flux at the reference foil to activation foil position, and off-energy neutron corrections. The reduced uncertainty is a good measure of how precisely we have measured the shape of the FPY data with respect to the incident neutron energy.

V. RESULTS

The cumulative FPY data reported here cover the range of incident neutron energies from 5.5 to 11 MeV, for ^{235}U, ^{238}U, and ^{239}Pu. These data complement that which was previously published by this same collaboration [7] in the region of first-chance fission (0.56–4.5 MeV) and at 14.8 MeV. In Ref. [7] are also results for 5.5 MeV from ^{239}Pu but not from either uranium target. In this publication we include the 5.5 MeV results from all three targets, and we have updated the ^{239}Pu data from Ref. [7] to include the new analysis methodology and corrections due to changes in reference foil masses described in Sec. II. Taken together, these data provide the excitation function for the energy dependence of more than a dozen high-yield fission products for the three major actinides with incident neutron energies from 0.5–14.8 MeV in approximately 1 MeV steps.

As discussed in the introduction, there are limited or no existing datasets in this second-chance fission energy region for the majority of fission products. This is especially true for ^{239}Pu, since ^{235}U and ^{238}U are easier to procure. Another reason for the lack of data in this region stems from the availability of neutron sources. Extensive datasets exist for neutron energies below 2 MeV, at thermal and in a fission spectrum, due to availability of reactors and critical assemblies for such measurements (see Fig. 1). Data near 14 MeV is also generally available due to the ease of use and cost for DT generators. Figures 8–10 show the scarcity of other literature data for ^{239}Pu in this region.

The major comparable datasets come from just a few sources: Chapman [24], Gindler [25], Glendenin [26], and Nagy [27]; the newest of which is from 1983. This presents the challenge of compiling a modern FPY database, and supporting future FPY evaluation efforts, using data with a 40 year gap for comparison. The datasets are mostly complete in this region in the sense there are a similar number of data points to the present measurements. However, none extend up to 11 MeV.

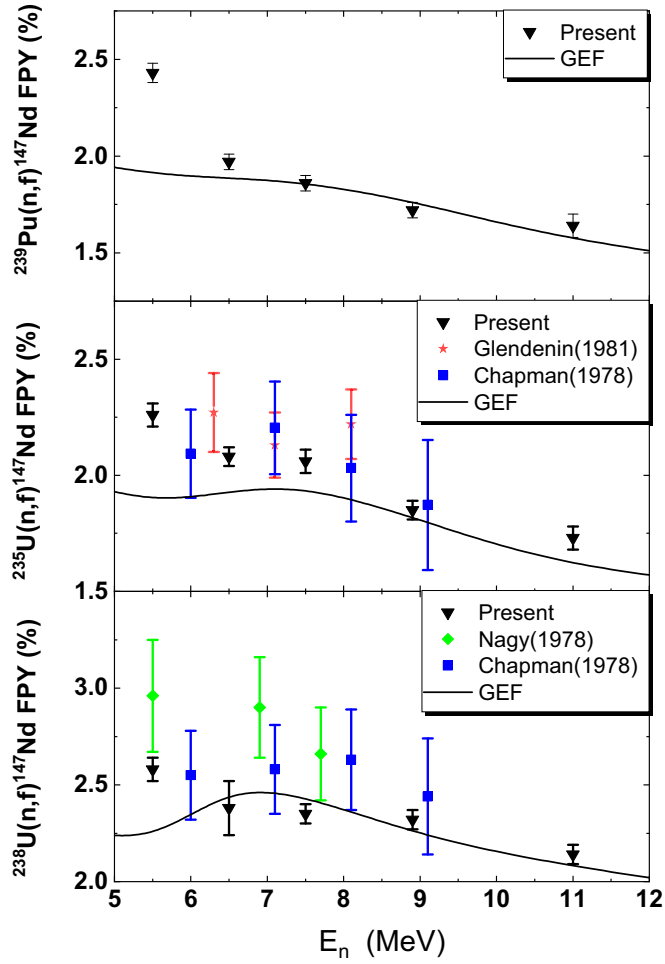

FIG. 8. Results for the cumulative fission yield of ^{147}Nd from ^{235}U, ^{238}U, and ^{239}Pu compared with existing data in the present energy region.

Tabulated results from these measurements can be found below in Tables VII, VIII, and IX. The results are given with their $\pm 1\sigma$ total uncertainty and then in parentheses the reduced uncertainty, described above in Sec. IV. Figures 8–10 show the current results for a select number of fission products compared with the existing literature data from the sources described above. The error bars represent the total uncertainties. As expected with increasing incident neutron energy, the fission yields show a steady decrease for all three targets for the peak-yield fission products. Considering a fission product near the valley such as ^{127}Sb, we observe a steady increase in the measured fission yield with energy (see Table VIII). The total uncertainties in the present data are also much less than the literature data, see Fig. 9, for example. The plotted fission products were chosen because they are all high-yield fission products with historical significance to the national laboratories.

The measured FPY distributions for ^{235,238}U(n, f) and ^{239}Pu(n, f) are compared with the semi-empirical general description of fission observables (GEF2021/1.1) model. The decrease of the FPYs in the second-chance fission region is also present in GEF calculations for all of the FPY under

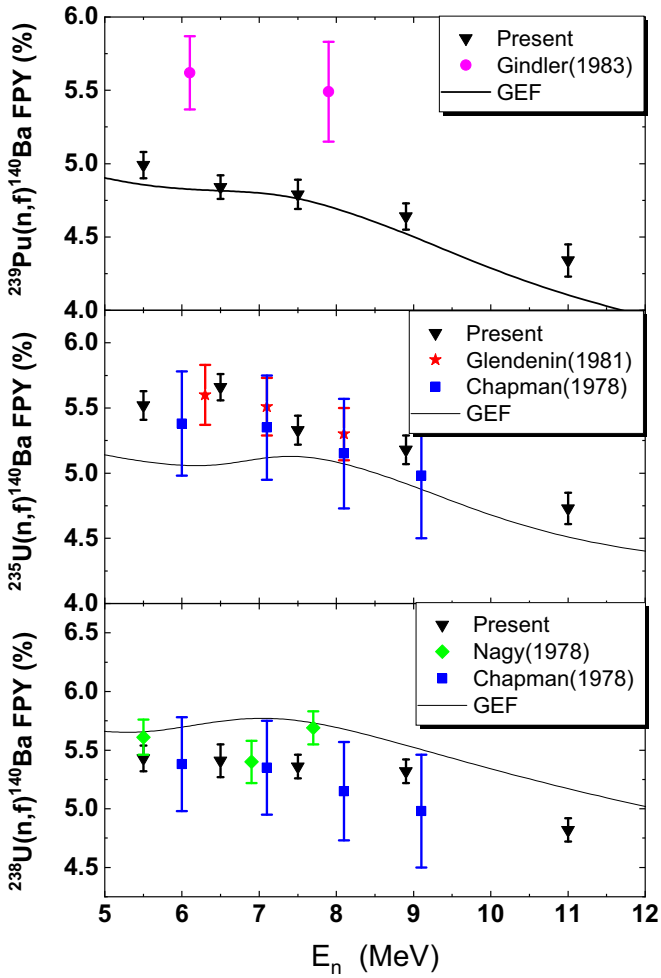

FIG. 9. Results for the cumulative fission yield of ^{140}Ba from ^{235}U, ^{238}U, and ^{239}Pu compared with existing data in the present energy region.

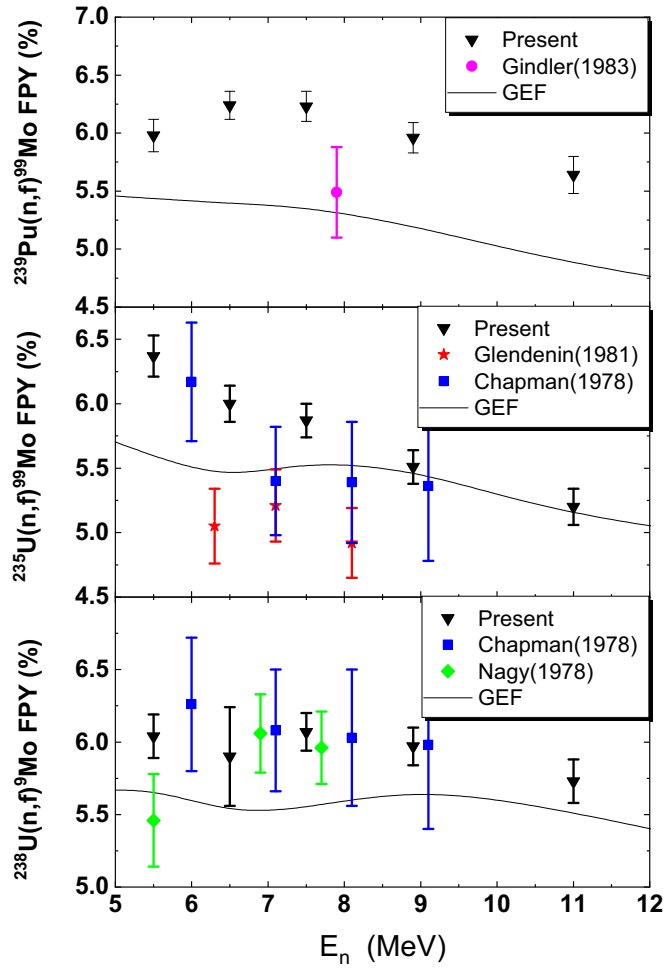

FIG. 10. Results for the cumulative fission yield of ^{99}Mo from ^{235}U, ^{238}U, and ^{239}Pu compared with existing data in the present energy region.

these studies. The calculations show a very good agreement for ^{147}Nd FPY for all fissioning systems and underestimation of the ^{99}MoFPY for ^{239}Pu(n, f), while it overestimated the ^{140}BaFPY for all three systems.

VI. SUMMARY

These FPY measurements represent the most extensive effort which our LANL-LLNL-TUNL Collaboration has accomplished to date. The FPYs in this work and Ref. [7] represent a complete set of data in the energy region from 0.5 to 15.0 MeV with fine-neutron-energy steps. It should be noted that our analysis was significantly improved relative to previous work [7], providing a more substantial basis for evaluating these cumulative FPY data for basic and applied physics. As has been described, many correction factors have been improved, such as the FC efficiency and kinematic boost, the Monte Carlo simulations of the neutron source and FC chamber geometry, detector efficiency, cascade summing, and others—increasing the fidelity of the current measurements. Additionally, the uncertainties associated with the parameters in Eqs. (1) and (3) were carefully quantified and updated to better reflect the precision of our measurements. Most importantly, with the corrected mass measurements of the fission chamber reference foils, shown in Table II, we have better agreement between existing datasets. Our previously published data in Ref. [7] will be updated to reflect the changes from these new mass measurements, as well as the improvements made in the analysis methodology in the near future. Once update is complete we will have one of the largest, complete, and self-consistent datasets of fission product yields spanning 0.5–14.8 MeV.

These new data in the mid-energy or second-chance fission region show a steady decrease as a function of incident neutron energy in the major FPYs. This is consistent with what would be expected from a monotonically decreasing function between the data at 4.5 and 14 MeV we previously measured [7]. The negative slope is due to the known increase in the symmetric fission mode with increasing incident neutron energy. There is no visible change or kink in the slope of these FPYs which might be affected by the third-chance fission opening up around $E_n = 11.0$ MeV.

ACKNOWLEDGMENTS

We wish to extend our gratitude to Mark Chadwick from LANL and Peter Bedrossian from LLNL for their encouragement and expertise in helping us to completing these measurements. We also would like to thank the technical staff at TUNL who maintained the accelerator capability. This work was supported by the US Department of Energy through the Los Alamos National Laboratory and Lawrence Livermore National Laboratory. Los Alamos National Laboratory is operated by Triad National Security, LLC, for the National Nuclear Security Administration of U.S. Department of Energy (Contract No. 89233218CNA000001). Lawrence Livermore National Laboratory under Contract No. DE-AC52-07NA27344. This work was also supported in part by the National Nuclear Security Administration Stewardship Science Academic Alliances Grants No. DE-NA0002936 and No. DE-NA0003884, and the U.S. Department of Energy, Office of Nuclear Physics, under Grant No. DE-FG02-97ER41033.

[1] O. Hahn and F. Strassmann, Über die Entstehung von Radiumisotopen aus Uran durch Bestrahlen mit schnellen und verlangsamten Neutronen, Naturwissenschaften **26**, 755 (1938).

[2] H. Selby *et al.*, Fission product data measured at Los Alamos for fission spectrum and thermal neutrons on ^{239}Pu, ^{235}U, ^{238}U, Nucl. Data Sheets **111**, 2891 (2010).

[3] J. Laurec *et al.*, Fission product yields of ^{233}U, ^{235}U, ^{238}U and ^{239}Pu in fields of thermal neutrons, fission neutrons and 14.7 MeV neutrons, Nucl. Data Sheets **111**, 2965 (2010).

[4] J. Lestone, Energy dependence of plutonium fission-product yields, Nucl. Data Sheets **112**, 3120 (2011).

[5] M. Chadwick *et al.*, Fission product yields from fission spectrum n $+^{239}$ Pu for ENDF/B-VII.1, Nucl. Data Sheets **111**, 2923 (2010).

[6] I. Thompson *et al.*, Evaluations of fission chain yields for ^{239}Pu from fission-spectrum neutrons, Nucl. Sci. Eng. **171**, 85 (2012).

[7] M. E. Gooden *et al.*, Energy dependence of fission product yields from ^{235}U, ^{238}U and ^{239}Pu for incident neutron energies between 0.5 and 14.8 MeV, Nucl. Data Sheets **131**, 319 (2016).

[8] J. Silano *et al.*, Characterization of ^{235}U, ^{238}U and ^{235}Pu fission ionization chamber foils by α and γ-ray spectrometry, Nucl. Inst. Meth. Phys. Res. Sect. A **1063** (2024).

[9] A. P. Tonchev, J. Silano, A. Ramirez, and R. Malone, Energy dependence of fission product yields, Technical Report LLNL-TR-839369 (Lawrence Livermore National Laboratory, 2020).

[10] C. Bhatia *et al.*, Dual-fission chamber and neutron beam characterization for fission product yield measurements using monoenergetic neutrons, Nucl. Instrum. Methods Phys. Res., Sect. A **757**, 7 (2014).

[11] IAEA Nuclear Data Services, https://www-nds.iaea.org, accessed July (2022).

[12] C. J. Werner, J. S. Bull, C. J. Solomon, F. B. Brown, G. W. McKinney, M. E. Rising, D. A. Dixon, R. L. Martz, H. G. Hughes, L. J. Cox, A. J. Zukaitis, J. C. Armstrong, R. A. Forster, and L. Casswell, MCNP Version 6.2 Release Notes (2018).

[13] J. Allison *et al.*, Recent developments in GEANT4, Nucl. Instrum. Methods Phys. Res. Sect. A **835**, 186 (2016).

[14] R. Vogt and J. Randrup, Detailed modeling of fission with FREYA, Nucl. Instrum. Methods Phys. Res. Sect. A **954**, 161225 (2020).

[15] G. Carlson, The effect of fragment anisotropy on fission-chamber efficiency, Nucl. Instrum. Methods **119**, 97 (1974).

[16] A. F. Sánchez-Reyes, M. I. Febrián, J. Baró, and J. Tejada, Absolute efficiency calibration function for the energy range 63–3054 keV for a coaxial Ge(Li) detector, Nucl. Inst. Meth. Phys. Res. Sect. B **28**, 123 (1987).

[17] K. Debertin and R. Helmer, *Gamma- and X-Ray Spectrometry with Semiconductor Detectors* (North-Holland, Netherlands, 1988).

[18] G. McCallum and G. Coote, Influence of source-detector distance on relative intensity and angular correlation measurements with Ge(Li) spectrometers, Nucl. Instrum. Methods **130**, 189 (1975).

[19] S. Sudár, *TruerCoinc: A Software Utility for Calculation of the True Coincidence Correction, Specialized Software Utilities for Gamma Spectrometry, No. IAEA-TECDOC-1275* (International Atomic Energy Agency (IAEA), 2002).

[20] ENSDF Database, http://www.nndc.bnl.gov/ensarchivals/.

[21] K. H. Schmidt, B. Jurado, C. Amouroux, and C. Schmitt, General description of fission observables, Nucl. Data Sheets **131**, 107 (2016).

[22] D. A. Brown *et al.*, ENDF/B-VIII.0: The 8th major release of the nuclear reaction data library with CIELO-project cross sections, new standards and thermal scattering data, Nucl. Data Sheets **148**, 1 (2018).

[23] G. Dietze and H. Klein, NRESP4 and NEFF4 Monte Carlo Codes for the Calculation of Neutron Response Functions and Detection Efficiencies for NE 213 Scintillation Detectors, Technical Report PTB-ND-22 (Physikalisch-Technische Bundesanstalt, Braunschweig, Germany, 1982).

[24] T. C. Chapman, G. A. Anzelon, G. C. Spitale, and D. R. Nethaway, Fission product yields from 6-9 MeV neutron-induced fission of ^{235}U and ^{238}U, Phys. Rev. C **17**, 1089 (1978).

[25] J. E. Gindler, L. E. Glendenin, D. J. Henderson, and J. W. Meadows, Mass distributions in monoenergetic-neutron-induced fission of ^{239}Pu, Phys. Rev. C **27**, 2058 (1983).

[26] L. E. Glendenin, J. E. Gindler, D. J. Henderson, and J. W. Meadows, Mass distributions in monoenergetic-neutron-induced fission of ^{235}U, Phys. Rev. C **24**, 2600 (1981).

[27] S. Nagy, K. F. Flynn, J. E. Gindler, J. W. Meadows, and L. E. Glendenin, Mass distributions in monoenergetic-neutron-induced fission of ^{238}U, Phys. Rev. C **17**, 163 (1978).